Measurement of phase gradients in the EEG

D.M. Alexander [a,b,*], C. Trengove [a,b], J.J. Wright [c], P.R. Boord [d], E. Gordon [a,d,e]

[a] *Brain Resource Company and Brain Resource International Database, PO Box 737, Broadway, Sydney, 2007 NSW, Australia*
[b] *Faculty of Information Technology, University of Technology, PO Box 123, Broadway NSW 2007, Australia*
[c] *The Liggins Institute, University of Auckland, 2-6 Park Avenue, Grafton 1001, Auckland, New Zealand*
[d] *Brain Dynamics Centre, Acacia House, Westmead Hospital, PO Box 533, Wentworthville, NSW 2145, Australia*
[e] *Brain Dynamics Centre, Westmead Millenium Institute and Department of Psychological Medicine, University of Sydney, PO Box 533, Wentworthville, NSW 2145, Australia*

Abstract

Previous research has shown that spatio-temporal waves in the EEG are generally of long spatial wavelength and form smooth patterns of phase gradients at particular time-samples. This paper describes a method to measure smooth phase gradients of long spatial wavelength in the EEG. The method depends on the global pattern of phase at a given frequency and time and is therefore robust to variations, over time, in phase-lag between particular sites. Phases were estimated in the EEG signal using wavelet or short time-series Fourier methods. During an auditory oddball task, phases across the scalp tend to fall within a limited circular range, a range that is not indicative of phase-synchrony nor waves with multiple periods. At times the phases tended to maintain a spatially and temporally ordered relationship. The relative phases were analysed using three phase gradient basis functions, providing a measure of the amount of variance explained, across the electrodes, by smooth changes in relative phase from a single minimum or single maximum. The data from 586 adult subjects were analysed and it was found that the probability of phase gradient events varies with time and frequency in the stimulus-locked average, and with task demands. The temporal extent of spatio-temporal waves was measured by detecting smoothly changing patterns of phase latencies across the scalp. The specific spatial pattern and timing of phase gradients correspond closely to the latency distributions of certain ERPs.
© 2006 Elsevier B.V. All rights reserved.

Keywords: Electroencephalogram; Brain dynamics; Phase gradient; Auditory oddball; Spatio-temporal waves

1. Introduction

1.1. Spatio-temporal waves in the cortex

Spatio-temporal waves in the gamma band have been measured in visual, auditory, somatic and olfactory areas of the cortex (Eckhorn et al., 2001; Freeman and Barrie, 2000). Related findings have been made for waves in the alpha band (Roelfsema et al., 1997).

In a review of earlier research on waves in the EEG, Hughes (1995a) suggest that abnormal mental states may be associated with alpha waves travelling in the posterior-anterior direction. EEG waves have also been described propagating from lateral to midline sites, or vice versa, depending on the subject's task (resting, calculation, emotional or pain experience; Hughes et al., 1995b). Ribary et al. (1991), using magneto-encephalogram (MEG), described an anterior to posterior spatio-temporal wave in the gamma band that occurs during the processing of auditory stimuli. In the EEG, anterior to posterior phase gradients in the alpha band have been recorded during a resting condition (Ito et al., 2005; Nunez et al., 2001). A posterior to anterior phase gradient in the alpha band has been recorded in response to steady state visual stimulation (Burkitt et al., 2000) and during a visual memorization task (Schack et al., 1999). Theta band travelling waves have been implicated in the transfer of visual information from long-term memory to working memory. Retrieval attempts are associated with an anterior to posterior wave motion, with a reversal to a posterior to anterior wave motion upon successful retrieval (Sauseng et al., 2002). Travelling waves have been detected during sleep that show a variety of behaviours, but more often originate in prefrontal–orbitofrontal regions and propagate posteriorly (Massimini et al., 2004).

* Corresponding author. Tel.: +61 2 9211 7120; fax: +61 2 9211 2710.
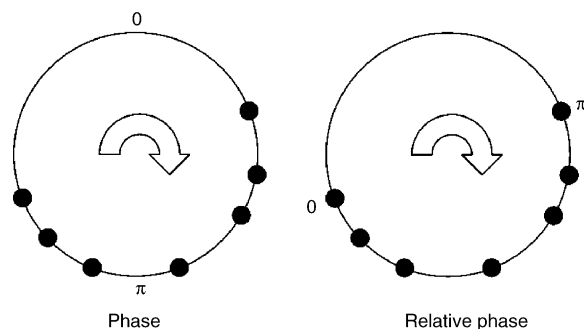*E-mail address:* dalex@brainresource.com (D.M. Alexander).

Fig. 1. Calculation of relative phase. Phases calculated at each electrode (for a given time-point and frequency) can be visualized on the unit circle – shown left of figure. The arrow shows the direction of phase change through time. The electrode that phase-leads the other electrodes into the largest gap on the unit circle is designated the phase-leading electrode. The relative phases are the phase at each electrode minus the phase of the phase-leading electrode – shown right of figure.

In a review of spatio-temporal waves in vertebrate and invertebrate brains, Ermentrout and Kleinfeld (2001) note that the phase gradient across the measurable region does not generally exceed π (i.e. the phase gradient comprises substantially less than one full cycle). This finding applies to waves at the scale of a Brodmann area in the cortex, but also to the global cortical spatio-temporal waves detected by Ribary et al. (1991), Sauseng et al. (2002, Fig. 1A and B), Massimini et al. (2004, Fig. 1, Figs. 1A, 4A and 5A) and Ito et al. (2005, Fig. 5). This property implies the waves described in this research have long spatial wavelength. Another important property of spatio-temporal waves described in this literature is that the pattern of phases, at a single time sample, change smoothly across the scalp. This property is apparent in the same set of figures just cited. The smoothness of the phase gradients associated with spatio-temporal waves suggests the latter may be detected via the former. That is, waves will be detectable from single snapshots of the dynamical activity. The long spatial wavelength of the waves suggests that the wave sources will also be measurable via phase gradients. One region will unambiguously phase-lead the rest even in a single snap-shot of the dynamics.

1.2. Estimation of phase

The phase of the EEG can be estimated at particular frequencies using Fourier methods. Long time-series Fourier-based methods are useful when the signal is relatively stationary, such as during steady state visual evoked potentials (Burkitt et al., 2000) or resting conditions (Nunez et al., 2001). Deviations from the assumption of stationarity, however, lead to smeared estimates of phase with long time-series methods (Schack et al., 1999). The study of event-related changes in phase therefore requires methods that are compact in both the time and frequency domains: short time-series Fourier methods using a sliding window (Haig et al., 2000), or wavelet analysis (Rodriguez et al., 1999; Yordanova et al., 2002). The timing of phase values of 0 and π can then be estimated by detection of minima and maxima in the filtered series (e.g. Sauseng et al., 2002; Yordanova et al.,

1998, 2002) or the centre phase value can be estimated for a given windowed time-series (e.g. Haig et al., 2000; Rodriguez et al., 1999).

The shortcoming of short time-series Fourier methods and wavelet analysis is that gains in temporal resolution of the phase estimate are paid for by loss of frequency resolution (i.e. an increase in bandwidth; Herrmann et al., 2005). In this respect, there is an important difference between the wavelet approach and Fourier methods (using a short but fixed window size). In the case of Fourier analysis, there is a fixed temporal and frequency resolution determined by the window size. By contrast, with wavelet analysis the temporal resolution and the frequency bandwidth scale proportionally with frequency (Herrmann et al., 2005). This property of wavelet analysis is suited to situations in which event-related variations in patterns of phase occur on a time-scale that scales inversely with frequency.

1.3. Phase gradient detection

Analysis of induced gamma oscillations in local field potentials (LFPs) in the monkey primary visual cortex has shown that spatially continuous waves can be present in multi-unit recordings despite variations in phase-lag between pairs of electrodes over the recording time (Eckhorn et al., 2001; Juergens et al., 1999). The variation in phase-lags can arise from changes in the spatial wavelength of the wave, by either (1) local variations in the spatial wavelength as the wave moves across the recording array, or (2) global changes in spatial wavelength over duration of the wave, or (3) differences in spatial wavelength of different wave-events whose characteristics are otherwise the same. The variations in phase-lag between recording sites can mask the presence of the continuous wave over large distances if a measure that assumes constant phase-lags is used. Spatially continuous cortical waves traverse distances four times greater than suggested by coherence measures, for example (Eckhorn et al., 2001; Juergens et al., 1999). The present research does not assume constant phase-lags in the method to detect spatio-temporal waves.

Phase topography in the EEG is generally calculated relative to the phase at a reference site, that is, a spatial ordering (e.g. Cz in Nunez et al., 2001; O1 and O2 in Schack et al., 1999; PO3 in Ito et al., 2005). Here we take a novel approach to calculating relative phase, in which the phases are referenced temporally to the leading part of the wave. Finding the phase-leading electrode is unambiguous provided the phase values lie within a range sufficiently less than 2π (e.g. $\sim\pi$ or $\sim 3\pi/2$). The phase-leading electrode is simply that electrode which phase-leads the rest of the electrodes in this range. Each electrode's phase is then calculated relative to the phase-leading electrode. This method has the advantage that the *temporal ordering* implicit in the phase gradient is preserved throughout subsequent analyses, allowing direct comparisons to explicit temporal measures such as latency gradients and ERP latencies.

There is a paucity of methods in the literature for characterizing EEG phase topography across the scalp. The most common method is to compare phases between electrode pairs (Rodriguez et al., 1999; Schack et al., 1999), but this approach is difficult

to apply to the detection of phase gradients, which are by their nature a global pattern. Burkitt et al. (2000) detected posterior to anterior phase gradients by means of a linear regression of phase values along midline sites. Sauseng et al. (2002) detected minima and maxima in filtered time-series, and followed their progression across the head along the anterior–posterior axis. The present research generalizes these approaches to two dimensions by choosing three *spatially smooth* basis functions, each having the property of containing only one maximum. These basis functions allow a wide range of *phase gradients* to be modelled. The fit of the relative phase data to the phase gradient model can also be calculated. The basis functions can also be applied to the analysis of latency gradients, measuring the time-course of the spatio-temporal waves in a similar fashion to Sauseng et al. (2002) and Massimini et al. (2004).

Analysis of the relative phase data from a population of subjects reveals event-related changes in the amount of variance accounted for by the phase gradient model. Smoothly changing phase gradients are associated with contraction of phases across the scalp to $\sim 2\pi/3$, that is, long spatial wavelengths. Measurement of latency gradients revealed that smooth phase gradients are indicative of spatio-temporal waves. The event-related timing and frequency properties of the phase gradients, as well as their specific direction across the scalp, suggest a close relationship to the latency topographies seen for a number of event-related potentials (ERPs).

2. Methods

2.1. Subjects

This study used the data of 586 adult subjects from the Brain Resource International Database. Subjects' ages ranged between 25 and 50, with approximately equal representation of male and female. All subjects gave written informed consent prior to participation, and local ethics committees for each participating laboratory approved all experimental procedures. Exclusion criteria for subjects were a history of brain-related illness (themselves or a first degree relative), substance abuse, neurological disorder or organic brain injury. Subjects were recruited from general metropolitan New York, Rhode Island, London, Nijmegen, Sydney and Adelaide.

2.2. Auditory oddball task

Subjects were presented with a series of high and low tones, at 75 dB and lasting for 50 ms, with an inter-stimulus interval of 1.0 s. The rise and fall times of the tones were 5 ms. Subjects were instructed to press buttons with the index finger of each hand in response to 'target' tones (presented at 1000 Hz). Subjects were asked not to respond to 'background' tones (presented at 500 Hz). Speed and accuracy of response were equally stressed in the task instructions. The background and target tones were presented in a quasi-random order, with the constraint that two targets cannot appear consecutively. There were 60 targets and 280 backgrounds. The duration of the auditory oddball task was 6 min.

2.3. EEG recordings

Participants were seated in a sound and light attenuated room. An electrode cap was used to acquire data from the Fp1, Fp2, F7, F3, Fz, F4, F8, FC3, FCz, FC4, T3, C3, Cz, C4, T4, CP3, CPz, CP4, T5, P3, Pz, P4, T6, O1, Oz and O2 electrode sites. Data were recorded relative to an additional cephalic electrode, but referenced offline to an average reference. Horizontal eye movements were recorded with electrodes placed 1.5 cm lateral to the outer canthus of each eye and vertical eye movements were recorded with electrodes placed 3 mm above the middle of the left eyebrow and 1.5 cm below the middle of the left bottom eye-lid. Skin resistance was less than 5 kΩ. A continuous acquisition system was employed and data was EOG corrected offline (Gratton et al., 1983). The sampling rate was 512 Hz. A low pass filter with attenuation of 40 dB per decade above 100 Hz was employed prior to digitization.

2.4. Numerical methods

The discrete Fourier transform (DFT) was used in a novel way to extract the phase $\phi(t,f)$ of the EEG signal at arbitrary frequencies and times for each series. For a given window of data of width T centred at time t only a *single* DFT component is used, being that of a given, fixed harmonic of index k corresponding to frequency $f = k/T$. Unlike the standard DFT usage, a range of frequencies is obtained by using a range of window sizes T. Note, this is essentially equivalent to a wavelet analysis and gives numerically similar results to Morlet wavelets (Herrmann et al., 2005).

The DFT component that is computed for the kth harmonic on a window $[t - T/2, t + T/2]$ is the discrete equivalent of the corresponding Fourier component of a continuous time-series $x(t)$, given by

$$H_{t,T}(k) = \int_{-T/2}^{T/2} \exp(2\pi i k \tau / T) w(\tau / T)[x(t + \tau) - \bar{x}_T(t)] \, d\tau$$

where

$$\bar{x}_T(t) = \frac{1}{T} \int_{-T/2}^{T/2} x(t + \tau) \, d\tau$$

Note that the DC component of the window, $\bar{x}_T(t)$, is subtracted from the time-series, and the result is then multiplied by a tapering function $w(\tau/T)$ defined to be zero except in the window $\tau \in [-T/2, T/2]$.

In practice, a discrete Fourier transform is used to compute $H_{t,T}(k)$ by sampling the interval $[t - T/2, t + T/2]$ at N points, with N chosen as a power of 2 so the standard fast Fourier transform (FFT) algorithm can be used. Arbitrary window sizes T (corresponding to arbitrary frequencies $f = k/T$) are achieved by down-sampling the 500 Hz raw data series to generate data sampled at rate N/T. Two different tapering functions were tried, with essentially no difference in results: a cosine taper (or Hanning window) $w(s) = (1/2)[1 + \cos(2\pi s)]$; a parabolic taper (or Welch window) $w(s) = 6(1/2 - s)(1/2 + s)$. The latter taper was used in the results reported herein.

The phase $\phi(t,f)$ is then given by the argument of the complex-valued quantity $H_{t,T}(k)$. Given the real and imaginary parts of $H_{t,T}(k)$ are a_k and b_k, respectively, the phase is calculated as follows, in order to fall in the range $[0, 2\pi]$:

$$\phi(t,\,f) = \tan^{-1}\left(\frac{b_k}{a_k}\right) + \pi H(-a_k) \bmod 2\pi$$

where the domain and range of $\tan^{-1}(b_n/a_n)$ are $[-\infty,+\infty]$ and $[-\pi/2,\pi/2]$ respectively and $H(x) = 1$ if $x > 0$; 0 otherwise.

At a given time and frequency, the phases across the 26 electrodes comprised by the vector $\Phi = (\phi_n)_{n=1,\ldots,26}$ were compared, and the largest gap in phases on the unit circle was determined. The electrode phase-leading the rest of the electrodes into this gap was designated the phase-leading electrode, l. Given the above definition of a Fourier component, the moving-window phase $\phi(t,f)$ of a pure sine wave signal $\cos(2\pi ft + \theta)$ of arbitrary initial phase θ *decreases* at constant rate. The phase-leading electrode is therefore the electrode with the larger phase value – relative to the phase values within the largest gap – of the two electrodes that bound this gap (see Fig. 1). The vector of relative phases $\Psi = (\psi_n)_{n=1,\ldots,26}$ can be defined, wherein the relative phase of each electrode was calculated by subtracting from its phase the phase of the phase-leading electrode:

$$\Psi_n = \phi_n - \phi_l \bmod 2\pi$$

The phase leading electrode as a matter of definition has a relative phase of zero. The spread of phases on the unit circle, $s_\Psi = \max_n \{\psi_n\}$, can be used as a measure of spread of phase lags.

2.5. Measuring phase gradients

Burkitt et al. (2000) have analysed posterior to anterior phase gradients by a linear regression of relative phases at the midline electrodes sites. An analogous procedure is to correlate the relative phases from all sites with an idealized two-dimensional (spherical) gradient of phase values that changes smoothly across the scalp. This is the strategy taken in the present research. Modelling and mathematical considerations suggest that a limited number of factors are able to explain most of the variance in measurements on a sphere, if the covariance between measurement sites is a function of recording site separation (Silberstein and Cadusch, 1992). Spatial covariance in scalp EEG measures is attributable to both real neurophysiological effects and volume conduction by the skull. Factor analysis of real and simulated EEG data produces similar factors: an anterior–posterior gradient, a circular gradient from the central, apex site to sites at the periphery of the scalp, and a left–right gradient (Duffy et al., 1990; Silberstein and Cadusch, 1992; Skrandies and Lehmann, 1990). Principle components analysis (PCA) analysis on relative phase data confirmed these factors (see Appendix A). These factors make suitable basis functions for detecting phase gradients in relative phases because each is smooth, has only a single maximum, and is orthogonal to the other basis functions (i.e. the pair-wise correlations are zero). When normalized to have vector length of 1 and mean values of 0, they form an orthonormal

basis for an idealised phase gradient space. The phase gradient basis functions used in the present research are illustrated in Fig. 2 (upper).

Using three basis functions with these properties, denoted B_{A-P}, B_{P-C} and B_{R-L}, allows a wide variety of phase gradients to be characterized by means of linear combinations of the basis functions. Some of the possible linear combinations are illustrated in Fig. 2 (lower). Any relative phase vector Ψ can be projected into this idealised phase gradient space to produce $M\Psi$, the phase gradient map of best fit, given by

$$M\Psi = \rho(B_{A-P}, \Psi)B_{A-P} + \rho(B_{P-C}, \Psi)B_{P-C}$$
$$+ \rho(B_{R-L}, \Psi)B_{R-L}$$

where $\rho(a,b)$ denotes the correlation of two vectors a and b. That is, $M\Psi$ is a weighted sum of the basis functions derived from the correlation of Ψ with each of the basis functions. Each $M\Psi$ has the property of being smooth with either a single minimum or a single maximum. The fit (amount variance explained) of $M\Psi$ to a given set of relative phases is

$$\sigma^2_{M\Psi} = \rho(M\Psi, \Psi)^2$$
$$= \rho(B_{A-P}, \Psi)^2 + \rho(B_{P-C}, \Psi)^2 + \rho(B_{R-L}, \Psi)^2$$

given the properties of the basis functions.

The detailed spatial patterns of phase gradient were also assessed. The correlations of each basis function with Ψ were calculated (denoted r_{A-P}, r_{P-C} and r_{R-L}). It is logically possible for symmetrically reversed patterns of phase gradient to be active at the same time and frequency in different trials (e.g. $M\Psi_{\text{trial } n} = B_{A-P}$ and $M\Psi_{\text{trial } m} = -B_{A-P}$). This results in an ambiguity if the trial-averaged r value for a given basis function is approximately zero, which could indicate an average of near zero r values or an average of high magnitude r values with opposite signs. The relative phases were therefore categorized in terms of the six maps derived from the basis functions and their reverse symmetries. The best map category $M_{\max}$ at a given time and frequency is given by

$$M_{\max} = \text{sign}(\rho(B_{\max}, \Psi))B_{\max};$$
$$M_{\max} \in \{+B_{A-P}, +B_{P-C}, +B_{R-L}, -B_{A-P}, -B_{P-C}, -B_{R-L}\}$$

where $B_{\max}$ is the basis function with the highest magnitude correlation with the relative phases:

$$|\rho(B_{\max}, \Psi)| = \max(|\rho(B_{A-P}, \Psi)|, \,|\rho(B_{P-C}, \Psi)|,$$
$$|\rho(B_{R-L}, \Psi)|)$$

This formulation for assessing specific spatial patterns of phase gradient does not depend on how well the best map category fits the relative phase data, merely that it is the best fit of the six choices.

The measures $\sigma^2_{M\Psi}$, r_{A-P}, r_{P-C}, r_{R-L} and $M_{\max}$ were calculated over 100 time samples per trial at 30 logarithmically spaced frequencies (1–16 Hz) and stimulus-locked averages computed for each time and frequency. The mean log power (MLP; mean over the electrodes of the logarithm of the power) was also calculated for each time and frequency. Values of mean $\sigma^2_{M\Psi}$ for
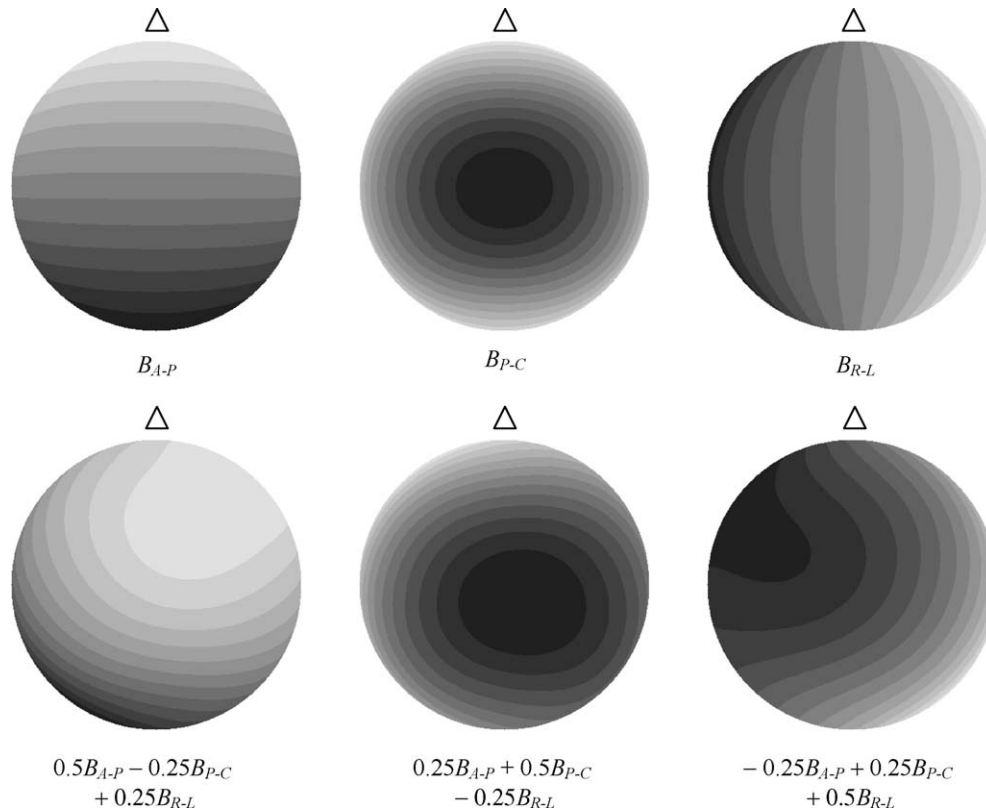
Fig. 2. Upper: the basis functions used to characterize phase gradient (light = phase leading; dark = phase lagging). Values between electrodes sites are interpolated for ease of interpretation. The nasal direction of the scalp is indicated with a small triangle. Lower: linear combinations of the phase gradient basis functions, showing some of the patterns of phase gradient that can be captured by the model. Each has only one maxima or one minima.

target and background trials were compared using multiple *t*-tests. Due to the large number of *t*-tests this entails, only time and frequency points where the significance level was $p < 0.001$ over six contiguous time or frequency points were accepted as statistically significant. Trial-averaged ERP wave-forms for each subject were also calculated and, for each electrode site, the latencies of the P2, N2 and P3 components were measured in the grand-average wave-forms.

2.6. Measuring latency gradients

Temporal waves were measured to assess the relationship between phase gradients and the wave motion described by Sauseng et al. (2002) and Massimini et al. (2004). For a given probe phase, p_ϕ (e.g. 0 radians), time intervals s_T were identified during which all electrodes passed through a value of p_ϕ once and only once. For each such interval s_T, each of the n electrodes could therefore be assigned a time, t_n, at which a phase value of p_ϕ occurred. The phase-leading electrode (ϕ_l) at the beginning of the interval s_T was assigned a latency $\tau = 0$, and other electrodes assigned latency values relative to the latency of this latency-leading electrode:

$$\tau_n = t_n - t_l$$

where t_l is the time at the beginning of the interval s_T. The vector of relative latencies can be defined as $T = (\tau_n)_{n=1,\dots,26}$. The variables s_T and T are directly analogous to s_Ψ and Ψ,

except that they refer to properties of latency gradients rather than phase gradients. By direct analogy with $\sigma^2_{M\Psi}$, the fit of the relative latencies to the basis functions can be computed:

$$\sigma^2_{MT} = \rho(MT, T)^2$$

σ^2_{MT} measures the goodness of fit of the relative latencies to a smoothly changing latency gradient having only one source or one sink.

Due to the long spatial wavelength of the waves (relative to the scalp), four probe phases were used (p_0, $p_{\pi/2}$, p_π and $p_{3\pi/2}$) to allow temporally extended waves to be detected. For convenience, the value of σ^2_{MT} at a given time sample was taken as the mean σ^2_{MT} generated by any of the four probe phases. The duration of a temporal wave was defined as the interval over which σ^2_{MT} was continuously greater than 0.64 (i.e. $r_{MT} > 0.8$). As defined here, a continuous temporal wave could markedly change its latency gradient over time, so long as the relative latencies maintained a good correlation to the basis functions (see Fig. 5A for an example of a wave with this property). Overwhelmingly this was not the case, however, and the short duration waves tended to engage in only a single pattern of relative latencies.

For each time sample within each interval s_T, we also calculated the goodness of fit of the relative latencies, T, to the idealized relative phase map, $M\Psi$, which is derived from the relative phases, Ψ. This statistic, $\rho(M\Psi,T)^2$, indicates the extent to which the specific spatial pattern phase latencies across the scalp

matches the idealized spatial pattern of relative phases derived from the linear combination of basis functions. It measures the extent to which the desired wave properties (spatially smooth, with only one source or one sink) apply *spatio-temporally*.

2.7. Testing methods using surrogate data

To test the ability of the above-defined measures to indicate the presence of spatio-temporal waves, as well as to validate their implementation, the methods were tested using surrogate data comprising random background waves with specific spatio-temporal waves superimposed. Thus at each electrode (i) the time-series took the form

$$x_i(t) = B_i(t) + \sum_w A_i^w(t)$$

The random background $B_i(t)$ at each electrode comprised, for each frequency f that was analysed (i.e. 1–16 Hz in 30 steps), a series of overlapping cosine-wavelets of frequency f and duration $4/f$ centred at a series of times t_j that give an inter-wavelet interval of $2/f$ plus jitter: $t_j = 2j/f + \varepsilon$ ($j = 0,1,2,\ldots$), where ε is a random variable uniformly distributed on the interval $(-1/f,1/f)$. Thus

$$B_i(t) = \sum_f \sum_j \cos(2\pi f(t - t_j))\, w((t - t_j)f/4)$$

where $w(s)$ is the cosine-taper window defined earlier.

A number of idealised wave components corresponding to idealised maps of the form $\Psi^w = a_w B_{A-P} + b_w B_{P-C} + c_w B_{R-L}$ were added to the randomized background. In addition to the basis map coefficients a_w, b_w and c_w, each travelling wave w was also specified by its frequency (f_w), time (t_w), duration (d_w) as a multiple of the period $1/f_w$, amplitude (A_w) and phase spread (s_w). Thus the wave component $A_i^w(t)$ at electrode i had the form:

$$A_i^w(t) = A_w \cos(2\pi f_w(t - t_w)$$
$$+ (s_w/s_{\Psi^w})\Psi_i^w)\, w((t - t_w)f_w/d_w)$$

Time-series of the form $x_i(t)$ were constructed for a number of trials, each with identical wave components against a randomized background. The parameter settings used in the reported results were $d_w = 3$, $A_w = 2$ and $s_w = 0.5$. These values for duration and amplitude of the surrogate wave, in combination with the cosine tapering, effectively meant the surrogate waves were detectable above the randomized background for approximately one cycle.

3. Results

3.1. Ordering of phases

Fig. 3 shows the phases (upper) and relative phases (middle) for subject 513 at 2.37 Hz during one trial. In this example, the phases tended to be arranged in order from anterior to posterior. This pattern is not atypical; episodes of phase contraction across the scalp were often associated with an apparent global spatio-temporal wave. During these episodes, a symmetry exists between phase and time. This symmetry is indicated by the

parallel diagonal lines in Fig. 3 (upper). Qualitative observation indicated that the ordering of phases could remain stable over fractions of a second, punctuated by sudden changes in phase relationships. The sudden changes in phase ordering were intermittent. At higher frequencies, the stable regimes of relative phase could continue for multiple periods. Referencing the phase via Cz (Fig. 3 lower) does not avoid the discontinuities seen in Fig. 3 (middle), although the discontinuities do take a slightly different form. The relative phases at some sites remain stable, but at other sites the relative phases make a sharp transition from π to $-\pi$ or vice versa.

The distribution of the spread of phases, s_Ψ, across all times, frequencies and subjects indicates that true synchrony is relatively rare – in the auditory oddball task at least. This distribution is shown in Fig. 4 (upper). An s_Ψ of $\pi \pm \pi/4$ or $3\pi/2 \pm \pi/4$ is much more common than $s_\Psi < \pi/2$. The distribution also indicates that in most cases ($\sim$75%) s_Ψ was less than $3\pi/2$. The distribution of s_Ψ calculated for 26 randomly generated phases is shown in black.[1] If the phases were random, a value of $s_\Psi < 3\pi/2$ would occur $\sim$1% of the time.

The distribution of s_Ψ is very similar across all frequencies tested (up to 42 Hz). The distribution of s_Ψ, ordered by frequency, is shown in Fig. 4 (middle). While a χ^2-test proved significant ($p < 0.001$) in our large dataset, visual inspection indicated that different frequencies had relatively minor variations of the same wedge-shaped distribution. Middle frequencies (beta) tended to have more peaked distributions at modal values of s_Ψ, while lower frequencies (delta–theta) and higher frequencies (gamma) showed a slight 'bulge' at $s_\Psi \approx 2\pi/3$. The similarity of the s_Ψ distributions across frequencies implies that behaviour of the phases, in terms of spread, was not strongly dependent on frequency.

Analysis of s_Ψ distributions at specific times post-stimulus reveals that the 'bulge' in s_Ψ at $s_\Psi \approx 2\pi/3$ is due to event-related contractions in s_Ψ, whereas the peak at $s_\Psi \approx 3\pi/2$ is not event-related. This effect is illustrated in Fig. 4 (middle), which shows the distribution of s_Ψ at 300 ms, 2 Hz for all subjects (see Fig. 6). At this time and frequency grand-average values of $\sigma_{M\Psi}^2$ were *moderately* high. The modal s_Ψ for this distribution is at approximately π. The effect of event-related changes in s_Ψ is further shown in Fig. 4 (lower), which compares s_Ψ for subject 47 at 6.78 Hz for two different times relative to stimulus onset. At 330 ms (where this subject had a *peak* in $\sigma_{M\Psi}^2$, see Fig. 6), the modal s_Ψ is $\sim$2$\pi/3$. This value of modal s_Ψ was typical for event-related peaks in $\sigma_{M\Psi}^2$ for individual subjects. At 800 ms the distribution of s_Ψ is peaked at $\sim$3$\pi/2$. These findings in relation to the behaviour of s_Ψ across frequencies and times support our original assumption that relative phases can be ordered by indexing the phases of each electrode relative to the phase-leading electrode. Most phase samples have an unambiguous gap in the phases, and this is especially the case during event-related decreases in s_Ψ.

---

[1] Note that these random phases were simply drawn from a uniform (circular) distribution, and not produced using the surrogate data generator described at the end of the methods section.
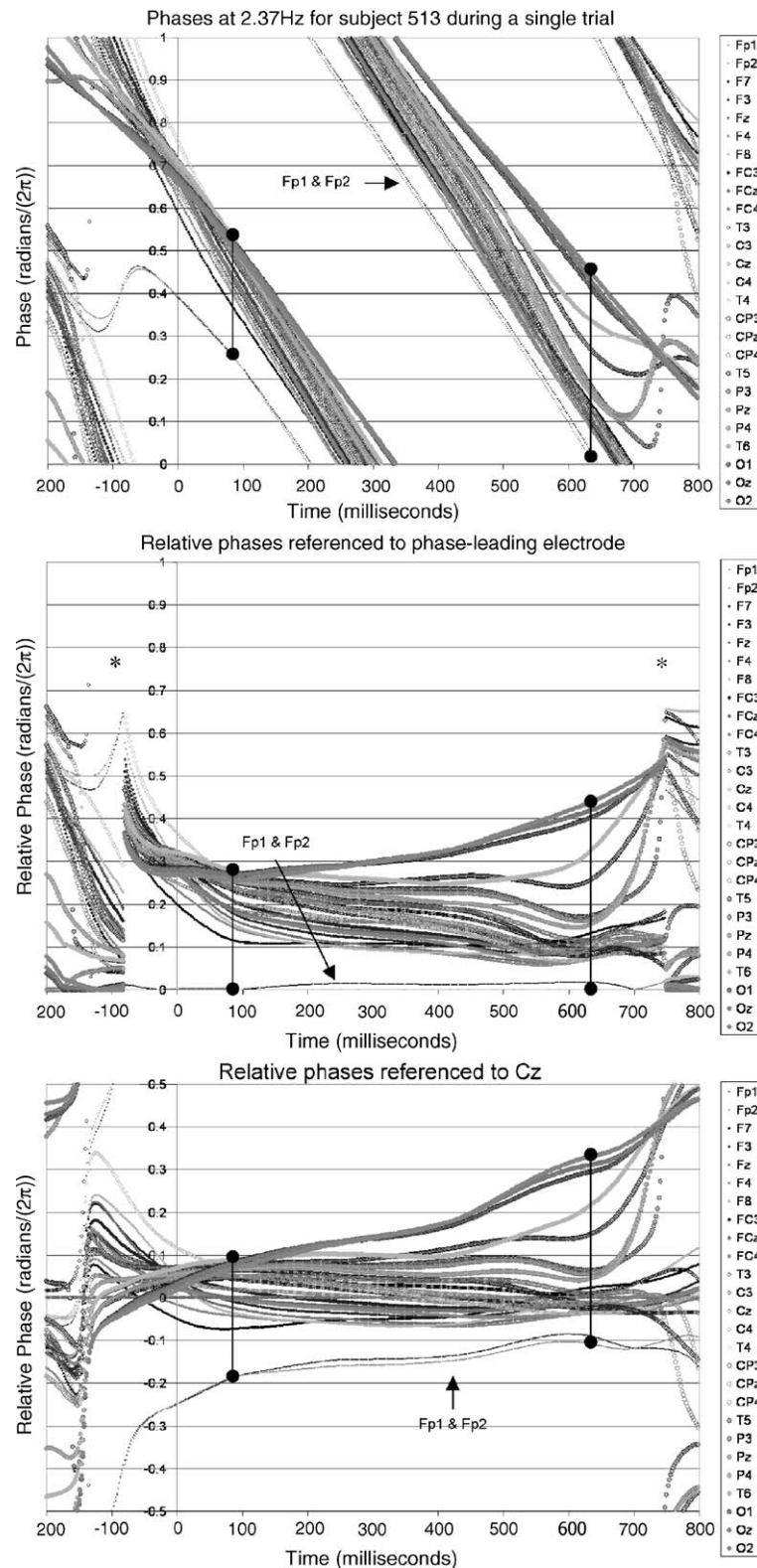
Fig. 3. Phases and relative phases of 26 electrodes at 2.37 Hz during a single trial for subject 513. Two measurements of s_Ψ are shown on each graph as black vertical lines with circular terminators. s_Ψ is given by the length of the lines. Upper: the raw phases at the 26 electrodes, as extracted by wavelet analysis. In this example, the phases for most time samples span a limited range, and they also tend to remain ordered relative to each other. In this case, the sites near the front of the scalp lead other sites (Fp1 and Fp2 are marked by arrows) during most of the time-series. Middle: the same data transformed into relative phases, referenced to the phase-leading electrode. In this view the stable ordering of the phases over time is more apparent. Another near universal feature seen in the relative phase data is also apparent: intermittent spikes in the spread of phases (marked with '*'). There was a strong tendency for re-orderings of phase to occur during these spikes in phase spread. Lower: the same phase data transformed into relative phases, referenced to the phase value at Cz. The same discontinuities in phase (marked with '*' in the middle graph) can be seen as some electrodes jump from $+\pi$ to $-\pi$ and vice versa.
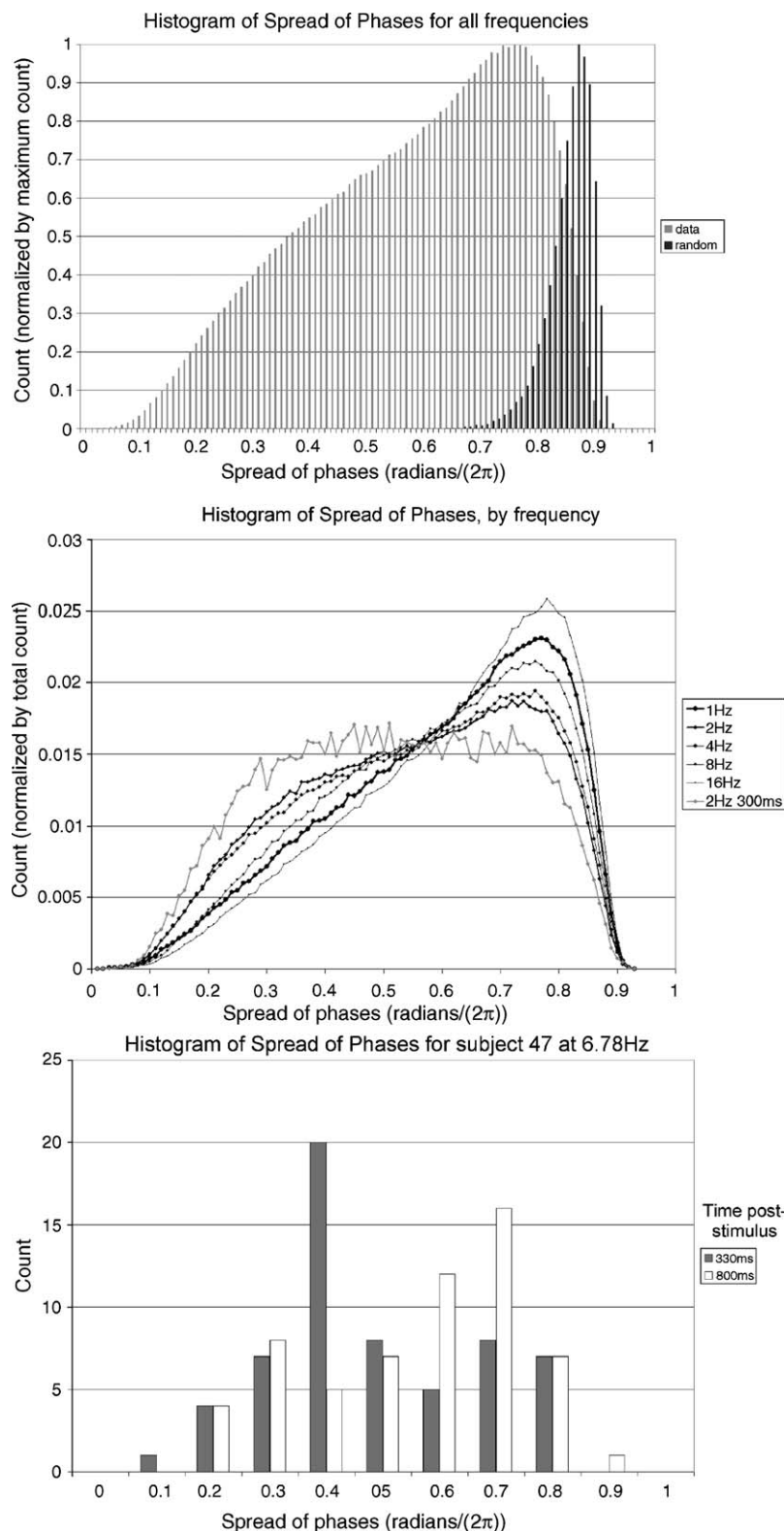
Fig. 4. Upper: the distribution (over times, frequencies and subjects) of the spread of phase, s_Ψ, is shown in grey bars. Most of the time, phase spread was less than $3\pi/2$, which suggests that the phases were not randomly distributed. Phase spread of less that $\pi/2$, indicative of near zero lag synchrony, was also not very common. The modal spread of phase $\sim 3\pi/2$ matches other experimental findings using various measures in different species, which have shown a spread of phases between $\pi/2$ and 2π. The distribution of spread of phases for randomly generated phases is shown in black bars. Middle: the distribution of s_Ψ (over all times) sorted by frequency. The distributions were quite similar regardless of frequency, suggesting that the degree of phase synchrony is not strongly frequency dependent. s_Ψ varies in an event-related fashion, shown by the distribution of s_Ψ for samples at 300 ms, 2 Hz. Lower: distribution of s_Ψ for subject 47 at their maximum trial-averaged $\sigma^2_{M\Psi}$ (330 ms, 6.78 Hz) and at a time sample when their trial-averaged $\sigma^2_{M\Psi}$ was low (800 ms, 6.78 Hz). The 'bulge' that can be seen in grand-average distribution of s_Ψ at $\sim 2\pi/3$ is due to event-related decreases in s_Ψ.

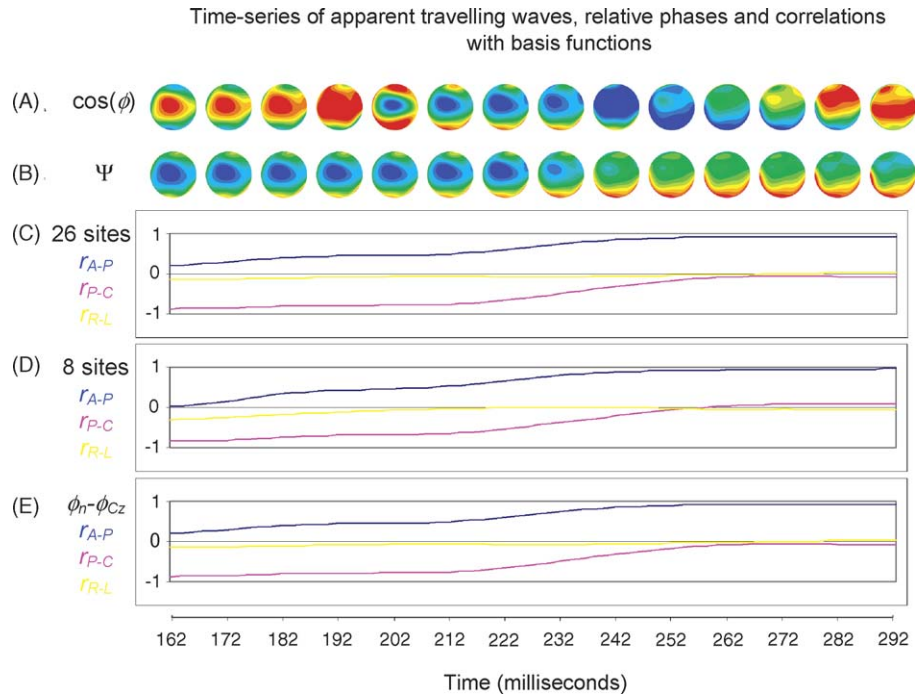Time-series of apparent travelling waves, relative phases and correlations
with basis functions

Fig. 5. Spatio-temporal waves at 9.92 Hz during a single trial for subject 126. (A) Scalp maps of activity due changes in phase during an spatio-temporal wave, i.e. $\cos(\phi)$. The scalp maps are taken at 10 ms intervals over 130 ms of a single trial. At first, a central to peripheral wave is apparent, which is replaced by an anterior to posterior wave. Values between electrodes have been interpolated for ease of interpretation (red = high activity; blue = low activity). An animation of this time-series is given is supplementary material A. (B) Scalp maps of relative phase for the same time samples as A. The relative phase measure reveals two basic patterns over the course of the time-series: a central to peripheral gradient and an anterior to posterior gradient. Values between electrodes have been interpolated for ease of interpretation (blue = phase leading; red = phase lagging). An animation of this time-series is given is supplementary material B. (C) Time-series of r_{A-P}, r_{P-C} and r_{R-L} over 130 ms of the same single trial. Initially the relative phases are negatively correlated with the peripheral to central basis function and then the relative phases become positively correlated with the anterior to posterior basis function. (D) Time-series of r_{A-P}, r_{P-C} and r_{R-L} calculated using a subset of eight electrodes (F7, Fz, F8, C3, C4, T5, Pz, T6). The minimum separation between these electrodes was ∼10 cm. The quantification of phase gradient pattern was very similar using this low spatial resolution electrode array. (E) Time-series of r_{A-P}, r_{P-C} and r_{R-L} calculated using 26 relative phase values referenced to Cz rather than to the phase-leading electrode.

3.2. Analysis of phase gradients and latency gradients

The pattern of scalp activations due to a spatio-temporal wave for subject 126 at a frequency of 9.92 Hz, is shown in Fig. 5. The uppermost part of the figure (A) shows the cosine of the phase at intervals of 10 ms over 130 ms. A wave of activity on the scalp moves from the centre of scalp to the peripheral sites and then the direction of motion changes to an anterior to posterior direction. During the wave motion, bands of synchronous activity can be seen running across the head in a direction orthogonal to the direction of wave motion. The second row (B) of scalp maps consists of the same time samples, but shows the relative phase values. The stability of this measure is illustrated clearly in that only two basic spatial patterns are seen: a central to peripheral gradient and an anterior to posterior gradient. The first set of time-series (C) shows the correlation of the relative phases with each of the phase gradient basis functions. The relative phases were initially negatively correlated with the peripheral–central basis function then positively correlated with the anterior–posterior basis function. The second set of time-series (D) show essentially the same information, except these correlations were between the relative phases of a subset of eight widely spaced electrodes (F7, Fz, F8, C3, C4, T5, Pz, T6) and versions of the phase gradient basis

functions using only this subset of electrodes. The long range patterns of zero-lag and non-zero-lag synchronous activity mean this smaller set of widely spaced electrodes is adequate to capture the spatial ordering and its persistence over the duration of the wave. The third set of time-series (E) shows the correlation between the three basis functions and the relative phases calculated relative to Cz rather than the phase-leading electrode. This set of time-series also provides essentially identical information.

The amount of variance, $\sigma^2_{M\Psi}$, explained by the linear combination of phase gradient basis functions, $M\Psi$, was averaged over target trials for subjects 47, 126, and 513. Time by frequency plots for these subjects are shown in Fig. 6. Event related changes in $\sigma^2_{M\Psi}$ were universal in all the individual subjects studied. Each individual typically had a low frequency component (2–3 Hz) between 250 and 500 ms and/or several mid-frequency components (6–16 Hz). The grand-average time by frequency plot of $\sigma^2_{M\Psi}$ for targets over 586 subjects is shown in Fig. 6. This plot shows two maxima of interest, one at ∼200 ms and ∼9 Hz and another at 300–400 ms and 2–3 Hz. A grand-average plot calculated using the subset of eight widely spaced electrodes is also shown in Fig. 6. The same qualitative pattern can be seen, although the low frequency phase gradients are more emphasized.
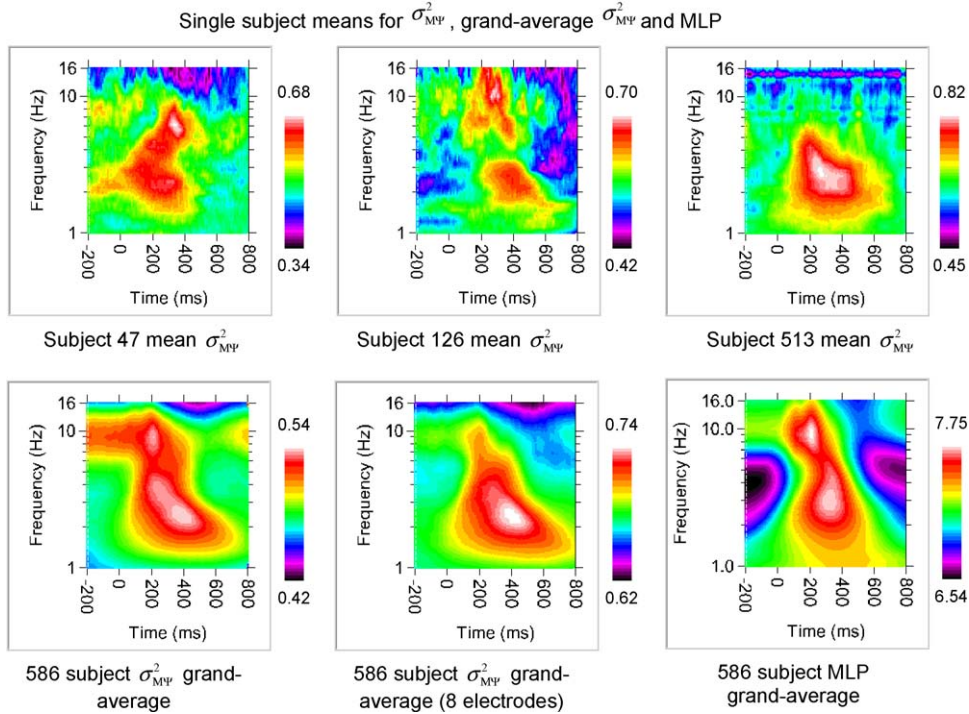
Fig. 6. Time by frequency plots of mean $\sigma^2_{M\Psi}$ for subjects 47, 126 and 513, grand-average plot of $\sigma^2_{M\Psi}$ for 586 subjects, grand-average plot of $\sigma^2_{M\Psi}$ calculated using only eight widely spaced electrodes and grand-average plot of MLP. The plots are scaled from the minimum value to the maximum value, with values shown on the colour scale to the right. Frequency is displayed on a logarithmic scale. The individual plots of mean $\sigma^2_{M\Psi}$ typically show a local maximum at $\sim$2 Hz between 250 and 500 ms and/or several local maxima between 6 and 16 Hz and 100–300 ms. The grand-average plots of $\sigma^2_{M\Psi}$ show two local maxima, one at $\sim$200 ms and $\sim$9 Hz and another at 300–400 ms and 2–3 Hz. Grand-average $\sigma^2_{M\Psi}$ calculated using only eight electrodes shows the same qualitative features as grand-average $\sigma^2_{M\Psi}$ for the full 26 electrodes, except that lower frequencies are more emphasized. The plot of grand-average MLP shows similarities to the grand-average plot of $\sigma^2_{M\Psi}$, however of the two maxima and two minima in grand-average MLP, only the maximum at $\sim$200 ms, $\sim$9 Hz shows an exact correspondence to grand-average $\sigma^2_{M\Psi}$.

The plots in Fig. 6 were produced using a two-cycle wavelet to extract the phase, as described in the methods section. The method therefore uses a very short time-window (i.e. twice the period of the frequency of interest), compared to other methods of analysing phase in the EEG with, for example, short time-series FFT (cf. Haig et al., 2000 use of a ten cycle FFT window and use of a similarly large number of cycles in Yordanova et al., 1998 and Kolev et al., 2002). To test the generality of our methods, the output for $\sigma^2_{M\Psi}$ was compared using one, two and five cycle wavelets. An additional analysis was also undertaken using a fixed window FFT of two seconds, in which the desired phases at each frequency were extracted from successively higher frequency bands within the same FFT analysis. These variations were tested with both the surrogate data generator and for grand-average subject data.

The results were robust over a range these variations, as shown in Fig. 7. As expected, the fewer the cycles in the wavelet function/FFT window, the better the time resolution. This gain was offset by poorer frequency resolution. When a larger number of cycles were used to extract the phase, the plots become blurred along the time axis but frequency resolution improved. When the number of cycles used to extract the phase greatly exceeded the number of cycles in the phase gradient events, the phase gradients events disappeared from the plots. This can be seen in the grand-average data as a decrease in the $\sim$2–3 Hz component in the five cycle wavelet and fixed window FFT plots, and

in the loss of the 9 Hz event in the fixed window FFT surrogate data plot.

A spatio-temporal wave is ordered in both space and time and the temporal properties of the waves were measured in the present research by σ^2_{MT}. Table 1 shows the detailed analysis of latency gradients in subjects 513, 47 and 126, at each of their peak frequencies for $\sigma^2_{M\Psi}$. The number of temporally defined waves was approximately one per trial over the 60 target trials. The definition of temporal waves in this paper was stricter than Massimini et al. (2004), because the temporal waves were required to traverse the entire scalp. The mean duration of the temporal waves was approximately the same at the three frequencies sampled. A consequence of this was that only at higher frequencies did waves with multiple temporal cycles appear, that is, waves that persisted for more than $1/f$ s. Values of $\rho(\sigma^2_{M\Psi}, \sigma^2_{MT})$, were greater than 0.75 in the three cases studied. When the latency gradient is smooth and has only one minimum or one maximum, this coincides with phase gradients having the same properties.

During episodes of temporally defined waves, the relative latencies can be fit to the specific spatial pattern of idealized phase gradients, $M\Psi$, derived from the relative phases. We calculated $\rho(M\Psi, T)^2$ for three subjects at their peak frequencies for $\sigma^2_{M\Psi}$, for all time samples during temporally defined waves in target trials. There was a close correspondence between the fit of the relative latencies to $M\Psi$ and the fit of the relative phases
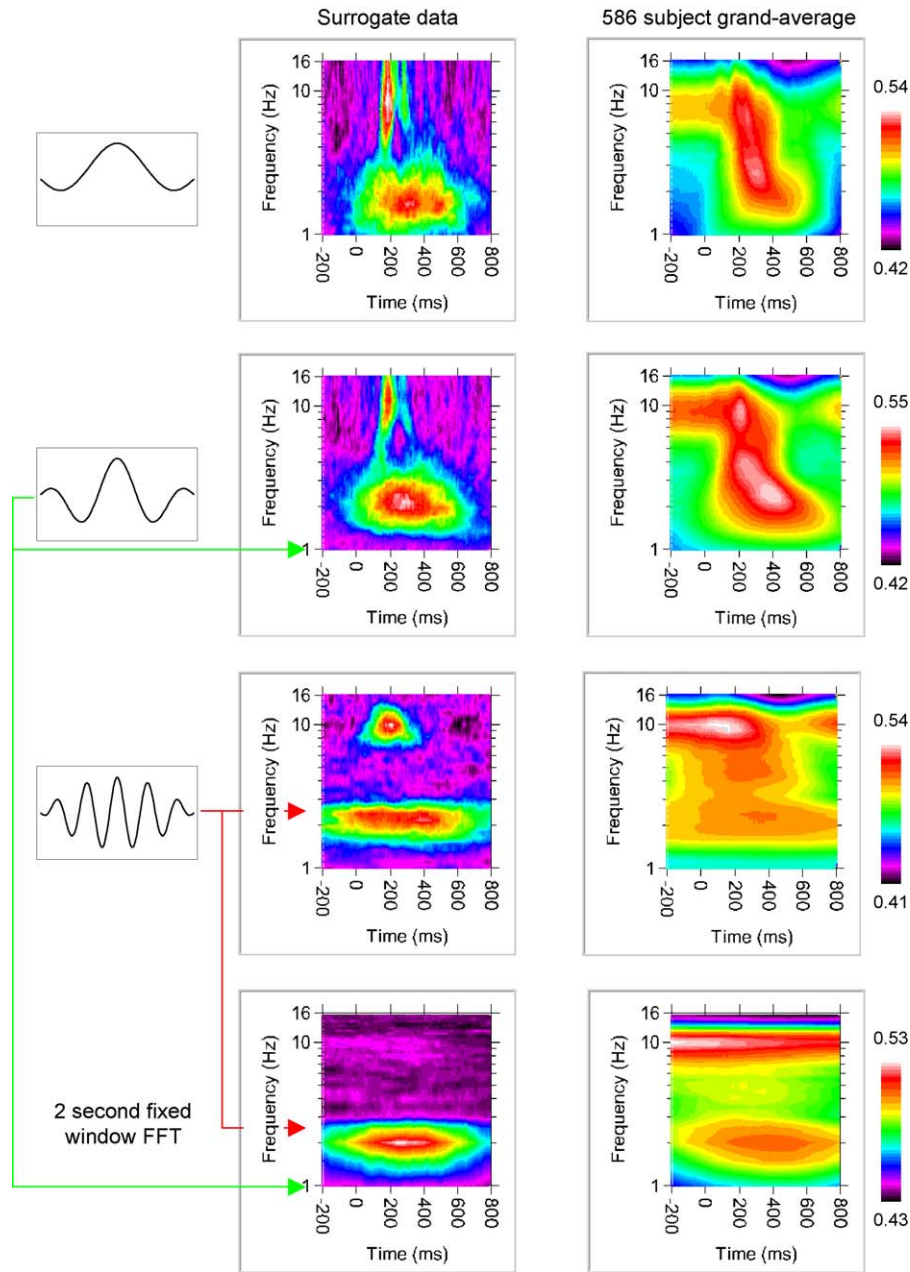
Fig. 7. Plots of $\sigma^2_{M\Psi}$ in which the phases were extracted using wavelet functions with different numbers of cycles or a fixed window FFT. The left column shows the output using surrogate data, with one travelling wave at 200 ms, 9 Hz and another at 300 ms, 2 Hz. Scales are not shown for surrogate plots because values are dependent on exact parameter values. The right column shows the grand-average $\sigma^2_{M\Psi}$ over 586 subjects. The phases were calculated using a (A) one, (B) two or (C) five-cycle wavelet function. The real valued part of the wavelet function is shown in each case. In (D), a fixed window of two seconds was used to calculate the phases via FFT. Note the linear scaling of centre frequencies in (D) (breaks in the dashed line on left edge of plot at 1, 2, . . ., 16 Hz), which are distorted logarithmically in the scaling of that axis. Red and green arrowed lines show the frequencies at which the wavelet analyses and FFT were equivalent. That is, extraction of the phase at 1 Hz using a two second windowed FFT is equivalent to using the two-cycle wavelet, and extraction of the phase at 2.5 Hz using a two second windowed FFT is equivalent to using the five-cycle wavelet. Similarly, extraction of the phase at 10 Hz using a two second windowed FFT is equivalent to using the 20-cycle wavelet (latter not shown).

to $M\Psi$. The strength of this relationship is illustrated in Fig. 8, in which data points can be seen to be scattered around the line $\rho(M\Psi, \text{T})^2 = \sigma^2_{M\Psi}$ (remembering that $\sigma^2_{M\Psi} = \rho(M\Psi, \Psi)^2$). In other words, specific patterns of latency gradient across the scalp can substitute equally well for the specific, coinciding, patterns of phase gradient across the scalp, when judged in terms of the linear combination of basis functions that best fit the relative phases. The specific phase gradients detected by the basis

functions are symmetrical in phase and time – they indicate spatio-temporal waves.

3.3. Task-related effects, specific spatial patterns of phase gradient and ERP latencies

Grand-average $\sigma^2_{M\Psi}$ plots were compared across task conditions – target versus background stimuli. Fig. 9A shows

Table 1
Statistics of temporally defined waves for three subjects at frequencies for which they had maximal $\sigma^2_{M\Psi}$

Subject	Frequency analyzed (Hz)	Number of waves	Mean duration (ms)	Proportion of waves with temporal cycle > 1	$\rho(\sigma^2_{M\Psi}, \sigma^2_{MT})$
513	2.37	63	98.7	0.0	0.81
47	6.78	57	102.5	0.09	0.75
126	9.92	76	83.0	0.17	0.85

The number of temporally defined waves was approximately one per trial (60 target trials), independent of the frequency. The mean duration of the waves also appeared to be independent of frequency. Consistent with the mean duration, the proportion of waves with duration of more than one temporal cycle increased with frequency. The fit of the relative phases to the basis functions was closely matched by the fit of relative latencies to the basis functions ($\rho(\sigma^2_{M\Psi}, \sigma^2_{MT}) \geq 0.75$). The plot of σ^2_{MT} vs. $\sigma^2_{M\Psi}$ is very similar to the plot of $\rho(M\Psi, T)^2$ vs. $\sigma^2_{M\Psi}$ shown in Fig. 8.

that background stimuli have negligible event-related changes. Related sampes t-tests for the 586 subjects reveal significant increases in $\sigma^2_{M\Psi}$ for the target condition across a broad range of frequencies post-stimulus.

Fig. 9B compares grand-average M_{max} counts for $+B_{A-P}$ and $-B_{A-P}$ maps with grand-average r_{A-P} values. There is a consistent set of relationships between the three plots, indicating that mean event-related increases in $+B_{A-P}$ count were associated with decreases in mean event-related $-B_{A-P}$ count, and vice versa. The same findings were made for the other basis functions (data not shown). This finding indicates that event-related increases in spatio-temporal waves of a particular direction of flow (at specific times and frequencies) *tended* to be unidirectional over trials and not flow in opposite directions from trial to trial. Mean values for r_{A-P}, r_{P-C}, r_{R-L}, and consequently mean $M\Psi$, do not suffer from the potential ambiguity discussed in Section 2.5.

The peaks in $\sigma^2_{M\Psi}$ for target stimuli arise at similar times to the latencies of the P2, N2 and P3 ERPs. The P2, N2 and P3 ERP latencies were calculated from the grand-average ERP time-series for the 586 subjects and the ranges for these ERP latencies across electrode sites were 169–198 ms, 206–276 ms and 315–356 ms, respectively. The ERPs had a latency distribution across the scalp that was parietal to peripheral for P2 and N2
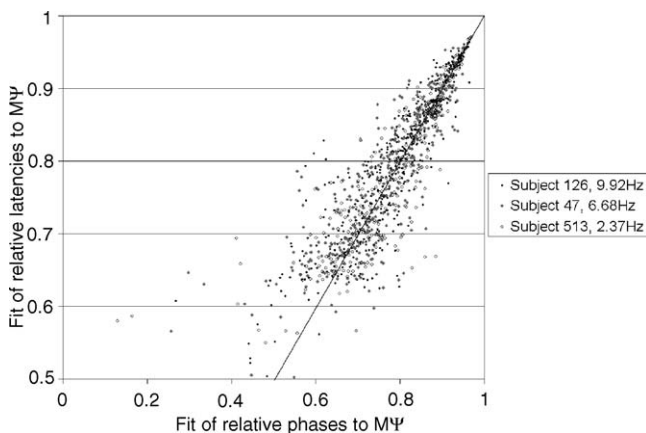

Fig. 8. Relationship between the fit of the relative phases to $M\Psi$ ($\sigma^2_{M\Psi}$) and the fit of the relative latencies to $M\Psi$ ($\rho(M\Psi, T)^2$) for three subjects at their peak $\sigma^2_{M\Psi}$ frequencies. Samples are taken from episodes during which temporal waves were detected, over all times and target trials. The graph shows that there was a close correspondence between the fit of the relative phases and the fit of the relative latencies to the linear combination of basis functions that best fit the relative phases. The line $\rho(M\Psi, T)^2 = \sigma^2_{M\Psi}$ is drawn for comparison.
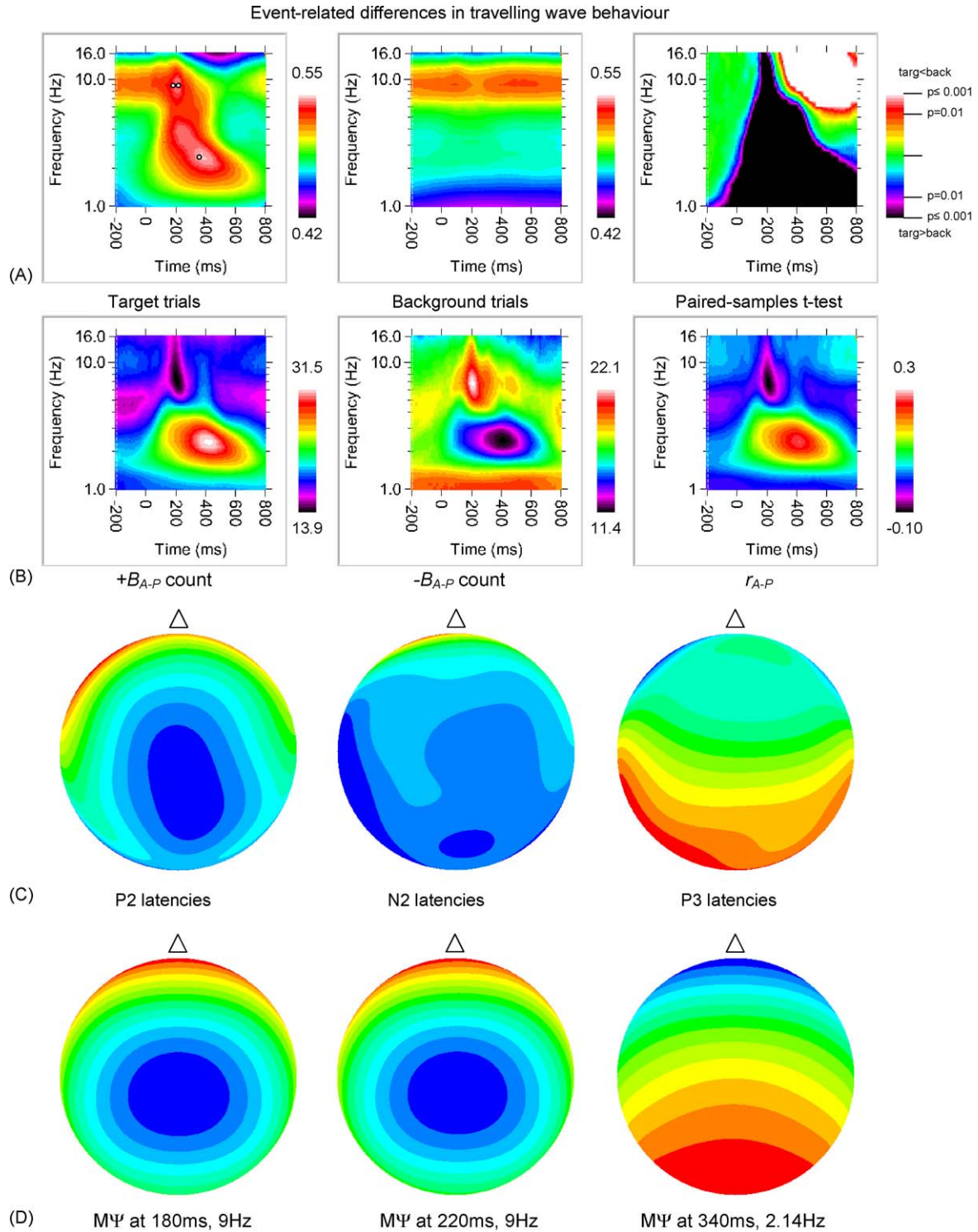
and anterior to posterior in the case of P3, shown in Fig. 9C. The mean latencies for these ERPs are marked on the grand-average $\sigma^2_{M\Psi}$ plot for target trials in Fig. 9A, at the $\sigma^2_{M\Psi}$ maximal for the mean latencies. Grand-average $M\Psi$ corresponding to these three time and frequency points are shown in Fig. 9D. At 180 ms (the mean of the P2 ERP latencies), 9 Hz (the peak $\sigma^2_{M\Psi}$ at 180 ms), the grand-average $M\Psi$ displayed a parietal to peripheral distribution of relative phases. At 220 ms (the mean of the N2 ERP latencies), 9 Hz (the peak $\sigma^2_{M\Psi}$ at 220 ms), the grand-average $M\Psi$ also displayed a parietal to peripheral distribution of relative phases. At 340 ms (the mean of the P3 ERP latencies), 2.14 Hz (the peak $\sigma^2_{M\Psi}$ at 340 ms), the grand-average $M\Psi$ displayed an anterior to posterior distribution of relative phases. The results show that the latencies of these ERP components across the scalp display a similar pattern to grand-average $M\Psi$ maps at peak $\sigma^2_{M\Psi}$ for times corresponding to the mean latencies of each ERP. Grand-average ERP latencies provide an independent measure of temporal ordering, a temporal ordering that shows qualitative similarities to the corresponding grand-average phase gradients.

3.4. Relationships between power and relative phase variables

The relationships of MLP with s_Ψ and $\sigma^2_{M\Psi}$ were analysed for subjects 126, 47 and 513, over all times and frequencies, shown in Table 2. MLP had a moderately strong negative correlation with s_Ψ (-0.47 to -0.68). Cross-correlation analysis of the data at frequencies of peak $\sigma^2_{M\Psi}$ for these three subjects showed that the correlation between MLP and s_Ψ was *strongly peaked at zero time-offset*, and of similar magnitude. The negative correlation between MLP and s_Ψ shows that during periods of low EEG power, the phases tended to be more evenly distributed on the unit circle. Some of this effect may be due to episodes of low power genuinely coinciding with episodes of EEG signal in which the phases are more evenly spread. However, some of this effect is likely due to measurement error in phase during periods of low power. At zero power phase is undefined. At low MLP the measured phases more closely approximate the case of randomly generated phases, which results in high values of s_Ψ (see Fig. 4, upper, black bars).

MLP had only a weak positive correlation with $\sigma^2_{M\Psi}$ (0.17–0.28) for subjects 126, 47 and 513. Cross-correlation analysis of MLP and $\sigma^2_{M\Psi}$ at frequencies of peak $\sigma^2_{M\Psi}$ for these three subjects revealed equivocal and variable relationships, with peaks not centred at time-offset zero. Episodes of high $\sigma^2_{M\Psi}$ are

Fig. 9. (A) Grand-average $\sigma^2_{M\Psi}$ values, over times and frequencies, for target and background stimuli. The background stimuli show no distinctive event-related features in the plot. The target stimuli have values of $\sigma^2_{M\Psi}$ that are significantly different from backgrounds over a wide range of times and frequencies post-stimulus. The small black circles indicate the times of mean latency for the P2, N2 and P3 ERPs, at maximal $\sigma^2_{M\Psi}$ for those times. (B) Comparison of grand-averaged M_{max} counts for $+B_{A-P}$ and $-B_{A-P}$ and grand-averaged r_{A-P} values. The three plots show the same features, except that $-B_{A-P}$ is inverted with respect to $+B_{A-P}$ and r_{A-P}, as expected. (C) Scalp latencies for P2, N2 and P3 ERP components computed from grand-average ERP time-series (blue = earlier; red = later). Values between electrodes sites are interpolated. (D) Grand-average $M\Psi$ values at 180 ms, 9 Hz and 220 ms, 9 Hz and 340 ms, 2.14 Hz, corresponding to the time and frequency points shown in (A) (left). The first and second scalp maps show a parietal to peripheral phase gradient, while the third shows an anterior to posterior phase gradient. The scalp latencies of the three ERP components shown in (C) are similar to the patterns of phase gradient in the corresponding $M\Psi$ maps.

Table 2
Relationships between EEG power and two phase-related variables, s_Ψ and $\sigma^2_{M\Psi}$

Subject	$\rho(\text{MLP}, s_\Psi)$	$\rho(\text{MLP}, \sigma^2_{M\Psi})$
126	−0.575	0.181
47	−0.47	0.173
513	−0.681	0.281

Power was calculated as the mean over the electrodes of the logarithm of the power (MLP). The relationships were calculated for three subjects, over all frequency and time samples. s_Ψ was moderately related to MLP, such that during episodes of low global power the spread of phase was large and during episodes of high global power the spread of phases was small. $\sigma^2_{M\Psi}$ was weakly related to MLP.

associated with moderately low s_Ψ ($\sim 2\pi/3$, see Fig. 4, lower), consistent with the weak positive correlation between MLP and $\sigma^2_{M\Psi}$. Grand-average event-related changes in MLP are shown in Fig. 6. The 2–3 Hz peak in MLP preceded the 2–3 Hz peak in $\sigma^2_{M\Psi}$ by almost 100 ms. By contrast, the ~ 9 Hz peak in MLP almost exactly coincided in time and frequency with the corresponding peak in $\sigma^2_{M\Psi}$. The two minima in the grand-average MLP plot coincided with fairly flat regions in the $\sigma^2_{M\Psi}$ plot. These findings are also consistent with the weak positive correlation between MLP and $\sigma^2_{M\Psi}$ and the equivocal results for cross-correlation between these variables.

To test the effects of low power on the estimation of phase and the detection of phase-gradients, we re-analysed the data of subjects 126, 47 and 513 at their peak frequencies (9.92, 6.78 and 2.37 Hz, respectively). The electrode with the minimum (log) power at each time sample was identified (min LP). The time-series for $\sigma^2_{M\Psi}$ using all samples were compared to the time-series for $\sigma^2_{M\Psi}$ after excluding the 10% of samples with the smallest min LP. Similar time-series were constructed by excluding the 20% of the samples with the smallest min LP. Excluding samples that contained electrodes with low power had negligible difference on the measurement of $\sigma^2_{M\Psi}$. The values of $\sigma^2_{M\Psi}$ were *marginally* higher at most time-points, but the overall pattern of $\sigma^2_{M\Psi}$ through time was essentially unchanged. This same analysis was repeated using a one-cycle wavelet to extract the phase, in order to maximise any effects of noise on estimation of phase. The effects of removing samples with low min LP were the same as when the standard two-cycle wavelet was used. Any noise in the estimation of phases, attributable to low power at individual electrode sites, did not have any effect on the detection of event-related *changes* in $\sigma^2_{M\Psi}$.

4. Discussion

4.1. Spatio-temporal waves in the EEG

This study analysed the spatial patterns of phase found in oddball EEG over a range of frequency bands. Like other measurements of spatio-temporal waves (Ermentrout and Kleinfeld, 2001), the spread of phases in the global EEG during the oddball task was generally between $\pi/2$ and $3\pi/2$. This distribution is not indicative of zero-lag phase synchrony over all sites or waves with multiple spatial cycles. The spread of relative phases varied in an event-related fashion, becoming more contracted

post-stimulus. Event-related contractions of s_Ψ during episodes of high $\sigma^2_{M\Psi}$ indicate waves of long spatial wavelength.

The chief result of the present research is that spatio-temporal waves in the EEG can be analysed as two-dimensional patterns of phase gradient, and that the amount of variance explained by the phase gradient model changes in an event-related fashion across a range of frequencies. The spatio-temporal waves remained highly ordered for a typical duration of 100 ms, indicated by analysis of latency gradients. There was also a symmetry in the dynamics between phase and time. The presence of the desired phase gradient properties (spatially smooth, with only one minimum or one maximum) coincided with waves that moved smoothly across the scalp in time, with one source or one sink. This was shown at the individual trial/frequency level, where specific patterns of latency gradients had a fit to $M\Psi$ approximately equal to the fit of the phase gradient patterns from which the $M\Psi$ were derived. At the level of grand-averaged data, there was a close correspondence between the scalp pattern of ERP latencies and the corresponding scalp pattern of grand-average $M\Psi$. The presence of phase gradients – as defined in this paper – is indicative of spatio-temporal waves.

The observed patterns of phases in EEG may arise in a number of ways. Massimini et al. (2004) regard slow-wave activity in sleep as travelling waves. This straightforward interpretation is rendered problematic for the present results by the finding that the spatial wavelength of the waves appears to be independent of temporal frequency. Theoretical formulation of unidirectional travelling waves in an electrocortical medium makes such a wave dispersion relation improbable (Rennie et al., 2000). Ribary et al. (1991) have suggested that related phenomena measured using MEG arise from thalamo-cortical scanning. A third potential mechanism, provided by Chapman et al. (2002), is based on the idea of destructive interference between multiple cortical sources. This latter framework unites a mechanism for the occurrence of synchronous fields, via constructive interference, with a mechanism for phase and latency gradients that have the appearance of travelling waves. The mechanism also allows for a distribution of apparent spatial wavelengths that are independent of frequency. Distinction among these competitive or complementary mechanisms is the subject of further research.

4.2. Numerical methods

The grand-average plots of $\sigma^2_{M\Psi}$ in Fig. 7 suggest that even using a one-cycle wavelet gives satisfactory results for detecting phase gradients. Indeed, because phase estimation is more prone to noise with fewer cycles in the wavelet function, a one-cycle wavelet provides a more stringent test of smoothness of phase gradient across the scalp. By contrast, use of windows with many cycles (more typical of Fourier methods) can be somewhat problematic if 'ringing' effects are artefactually introduced. In addition, the focus of the present research is on event-related changes in phase gradient. Because the temporal ordering of relative phases does not typically exceed one cycle (see Section 3.2), wavelets with low temporal resolution typically sample multiple changes in phase gradient behaviour. The gains in frequency resolution are therefore offset by an ambiguity as to

which event in time is being resolved with such frequency precision. The effect of event blurring can be seen clearly in Fig. 7, in the plots that use five cycle wavelets or the fixed window FFT (at the higher frequencies). Phase gradient events that last no longer than a cycle can disappear from the output altogether. Event blurring is also the likely cause of the differences in $\sigma^2_{M\Psi}$ plots for targets and backgrounds that are apparent for time-points prior to stimulus delivery at low frequencies. The use of two cycle wavelet functions in analyses therefore provides a good compromise between a variety of factors in the present research context.

The procedure for measuring phase gradients in the present research was guided by the insight that jitter in phase relationships between sites over time can disguise the presence of smooth, continuously propagating waves (Eckhorn et al., 2001). As defined in this research, a wave need only maintain a consistent spatio-temporal *ordering* of phases across sites, not a set of *constant* relative phase *values*. The use of correlational methods on relative phases to assess phase gradients means the measures are not affected by variations in s_Ψ, *ceterus paribus*. This allows a spatio-temporal wave to vary in spatial wavelength over time, and concomitantly, pairs of sites to vary in their relative phase, without altering the measure of fit to the phase gradient basis functions, $\sigma^2_{M\Psi}$. The relative phase/correlational methods are also fairly robust to local variations in the rate of change of phase gradient over the scalp. For example, a Ψ with a linear gradient across the scalp will give similar $\sigma^2_{M\Psi}$ to a Ψ with a monotonic but nonlinear gradient, *ceterus paribus*.

Analysis of latency gradients indicated a close relationship between the waves measured via phase gradient basis functions and temporally defined waves of the type described by Sauseng et al. (2002) and Massimini et al. (2004). The advantage of using phase gradients to detect spatio-temporal waves is that an estimate of fit to the phase-gradient model can be provided for each and every time sample, based only on a single time sample. Temporally defined wave measures require wave components to be tracked through time. The difference in techniques is analogous to identifying waves on a pond from either a single photograph or by analysing the motion of the water surface through successive frames of a movie.

4.3. The effects of volume conduction

The basis functions used to analyse phase gradients can arise as factors in factor analysis purely as the result of volume conduction effects, or as the result of spatial covariance in the underlying electrophysiology (Silberstein and Cadusch, 1992). A number of findings suggest phase gradient episodes (high $\sigma^2_{M\Psi}$) cannot be attributed volume conduction effects.

1. Spatio-temporal waves have been measured at the scale of the Brodmann area using LFPs (Eckhorn et al., 2001; Freeman and Barrie, 2000) and at the whole cortex scale using MEG (Ribary et al., 1991), methods which are not subject to smearing by volume conduction effects.
2. The measured phase gradients have a long spatial wavelength (greater than the 28 cm of maximum electrode separation)

and are comprised of bands of synchronous activity traversing the entire scalp. Volume conduction effects decay quickly past 2 cm and are negligible at 10 cm (Nunez et al., 2001; Rodriguez et al., 1999). Volume conduction therefore contributes a relatively localized blurring to the global phase gradient patterns measured at the scalp. Measurements of phase gradient using low spatial resolution electrode arrays, appropriate to the resolution of the scalp-smeared signal, replicate the results found using 26 electrodes.

3. Volume conduction is essentially instantaneous compared to the velocity of the spatio-temporal waves. While volume conduction causes a spatial smearing, it has no effect on temporal covariance. The spatio-temporal nature of the waves lends weight to the proposition that the spatial phase gradients are not merely the product of spatial smearing by volume conduction.

4.4. Relation to evoked response potentials

Stimulus-locked averaging of phase gradient events revealed distinctive event-related patterns dependent on task demands – namely auditory targets versus backgrounds. The 300–400 ms timing of the 2–3 Hz peak in $\sigma^2_{M\Psi}$ for target trials overlaps with the 315–356 ms latency of the P3 oddball ERP in grand-average curves. The low frequency characteristics of the P3 fit with this interpretation of the P3 as a 2–3 Hz wave (Basar-Eroglu et al., 1992; Demiralp et al., 1999). The P3 has an anterior to posterior latency distribution (Anderer et al., 1990), confirmed by the analysis of our own ERP data. The grand-averaged $M\Psi$ at the relevant time and frequency matched this latency distribution. The 300–400 ms, 2–3 Hz peak in $\sigma^2_{M\Psi}$ for target trials therefore incorporates the timing, frequency, latency pattern and task characteristics of the P3 ERP. A similar set of correspondences apply to the ∼200 ms, ∼9 Hz peak in $\sigma^2_{M\Psi}$ and the P2 and N2 ERPs. Future research will further explore the relationship between spatio-temporal waves and ERPs across a range of experimental paradigms.

4.5. Functional significance

The function of spatio-temporal waves in the cortex is unclear (Ermentrout and Kleinfeld, 2001), but they comprise an excellent candidate mechanism for the general process of global brain coordination. We speculate that they may be involved in the distribution of previous cognitive outcomes to all parts of the cortex, and/or consistency maintenance over multi-modal functioning. As described in the introduction and in the results section, spatio-temporal waves behave in an event-related fashion that varies systematically depending on task demands.

Spatio-temporal waves may also provide indicators of deviation from normative brain function. Phase gradient measures have been used to distinguish children with attention deficit/hyperactivity disorder from matched controls (Alexander et al., 2005). Patterns of spatio-temporal wave activity, measured in scalp EEG, showed specificity across a number of clinical groups: attention deficit/hyperactivity disorder, first episode psychosis and Alzheimer's disease. Phase gradient measures have

also been used to predict cognitive decline in elderly subjects with subjective memory complaints (Alexander et al., 2006).

Acknowledgements

Appendix A

The relative phases were analysed using PCA. PCA indicated that much of the variance in the relative phases during the oddball task could be accounted for by a limited number of factors.

The relative phases across all times, frequencies and subjects were randomly subsampled to reduce the data-set to 3×10^6 samples. Factor analysis produced essentially identical results to PCA in all cases mentioned here. The construction of surrogates by random permutation of electrode labels indicated a single factor on which all electrodes loaded evenly i.e. all high versus all low. This factor was due to the variation in s_Ψ and the distribution of relative phases within the range s_Ψ (i.e. the distribution was not normal or uniform, but peaked at 0 and s_Ψ). The remaining factors in the surrogate data explained negligible variance (<1%). Due to the predominance of a single factor in the surrogate data, we performed PCA on the *ranked* relative phases. A scree test (Fabrigar et al., 1999) and parallel analysis (Horn, 1965; Humphreys and Ilgen, 1969) on the PCA using ranked relative phases indicated a cut-off at three factors.

Based on these results it was concluded that for the oddball task, much of the variance in relative phases could be explained by three factors. The three factors were respectively characterised by phase gradients across the scalp from anterior to posterior, right to left and periphery to centre. The three factors are shown in Fig. 10.

Rotated PCA solutions were examined, but added no useful further information. Further, the results obtained without factor rotation showed simple correspondences to standard ERP latencies (see Section 4). If the PCA was performed on the unranked relative phases i.e. with a non-uniform distribution, the first three factors found were essentially identical to those found using ranked relative phases. Restricting PCA analyses to data with $s_\Psi < 3\pi/2$ or $s_\Psi < \pi$, or normalizing the range of
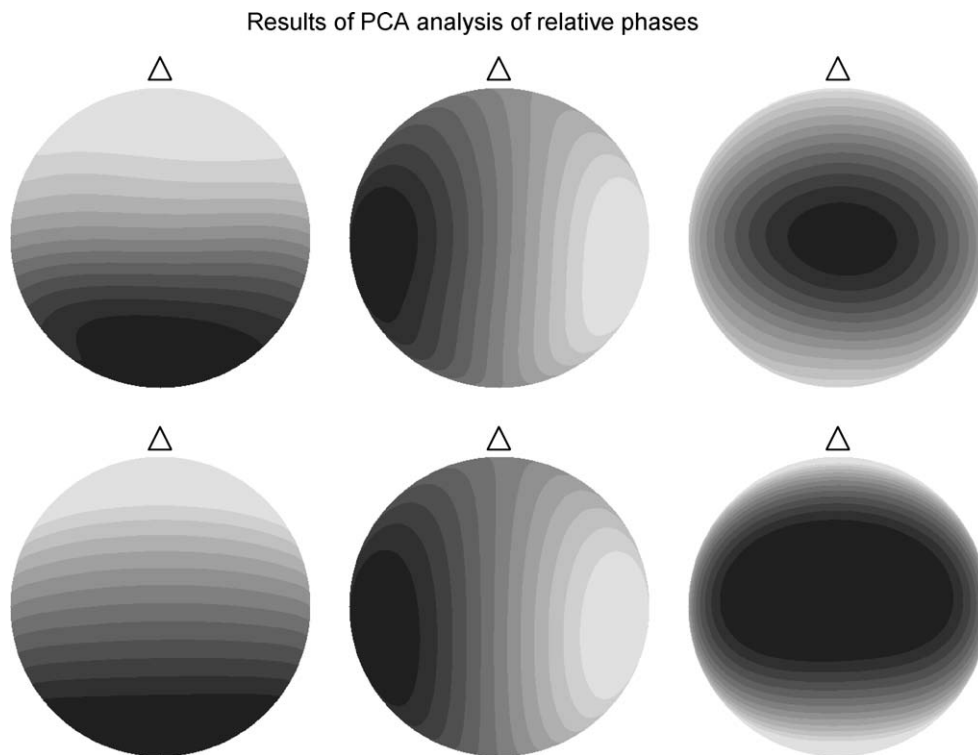

Fig. 10. Upper: factors arising from PCA analysis of ranked relative phase data, pooled across subjects, frequencies and times (triangle indicates nasal direction). The eigenvectors are ordered according to their eigenvalues. The anterior to posterior map (light = phase leading; dark = phase lagging) accounted for 29% of the variance, the right to left map 12% and the central to peripheral map 10%. PCA with unranked relative phase data produced the essentially identical maps for the first three eigenvectors, although the ordering (in terms of variance explained) was different. Lower: factors arising from PCA analysis of ranked relative phase data from eight electrodes only (F7, Fz, F8, C3, C4, T5, Pz, T6). Due to the lower dimensionality of this dataset, the amount of variance explained by the three factors was substantially greater.

relative phases by s_Ψ did not alter the types or number of factors found. Likewise targets and backgrounds, when analysed separately, produced essentially identical factors. Analysis of data from several other experimental paradigms (e.g. one-back working memory task) also produced these same factors. Referencing the relative phase to Cz rather than the phase-leading electrode also produced essentially identical results.

Another result of interest is that these three factors arise at all frequencies tested – from delta to gamma. There were some minor variations, but essentially the same factors (and no others) arise at each frequency. This does not mean that the same phase gradient (e.g. anterior to posterior) occurred simultaneously over a wide range of frequency bands. PCA and canonical correlation analysis of PCA factor by frequency interactions indicated only a weak tendency for adjacent frequency bands to be associated with the same factor at the same time (data not shown). This is also confirmed by the event-related time by frequency plots of $\sigma^2_{M\Psi}$ shown in Section 3.2. Similar factors arise at disparate frequencies, but this does not imply the same patterns of phase gradient occur simultaneously at disparate frequencies.

The PCA factors for relative phase are influenced by volume conduction effects of the skull and other tissue, since similar maps found in the measurement of EEG power using high resolution electrode arrays have been attributed primarily to volume conduction effects (Silberstein and Cadusch, 1992). In order to assess the relevance of volume conduction effects to our results, we repeated the PCAs using only a subset of eight electrodes (F7, Fz, F8, C3, C4, T5, Pz, T6). These sites have a minimum electrode separation of ∼10 cm. Since volume conduction effects drop off significantly after 2 cm and are negligible at 10 cm (Nunez et al., 2001; Rodriguez et al., 1999), the resulting factors will be much less influenced by volume conduction. The PCA factors using the low resolution array are shown in Fig. 10. The factors are qualitatively similar to the factors found using 26 electrodes.

Appendix B. Supplementary data

Supplementary data associated with this article can be found, in the online version, at doi:10.1016/j.jneumeth.2006.02.016.

References

Alexander DM, Arns MW, Paul RH, Rowe DL, Cooper N, Esser AH, Fallahpour K, Stephan B, Heesen E, Breteler R, Williams LM, Gordon E. EEG markers for cognitive decline in elderly subjects with subjective memory complaints. J Integr Neurosci 2006;5(1):49–74.

Alexander DM, Trengove C, Clark CR, Clark S, Kohn M, Williams LM, Gordon E. Apparent travelling waves in scalp EEG reveal a decrease in slow-wave activity for ADHD across several experimental paradigms. In: Proceedings of the 15th Australasian Psychophysiology Conference; 2005. p. 17.

Anderer P, Semlitsch HV, Saletu B. Multichannel auditory event-related brain potentials: effects of normal aging on the scalp distribution of N1, P2, N2 and P300 latencies and amplitudes. Electroencephalogr Clin Neurophysiol 1990;99(5):458–72.

Basar-Eroglu C, Basar E, Demiralp T, Schurmann M. P300-response: possible psychophysiological correlates in delta and theta frequency channels. A review. Int J Psychophysiol 1992;13(2):161–79.

Burkitt GR, Silberstein RB, Cadusch PJ, Wood AW. Steady-state visual evoked potentials and travelling waves. Clin Neurophysiol 2000;111(2):246–58.

Chapman CL, Bourke PD, Wright JJ. Spatial eigenmodes and synchronous oscillation: coincidence detection in simulated cerebral cortex. J Math Biol 2002;45:57–78.

Demiralp T, Ademoglu A, Schurmann M, Basar-Eroglu C, Basar E. Detection of P300 waves in single trials by the wavelet transform (WT). Brain Lang 1999;66(1):108–28.

Duffy FH, Jones K, Bartels P, Albert M, McAnulty GB, Als H. Quantified neurophysiology with mapping: statistical inference, exploratory and confirmatory data analysis. Brain Topogr 1990;3(1):3–12.

Eckhorn R, Bruns A, Saam M, Gail A, Gabriel A, Brinksmeyer HJ. Flexible cortical gamma-band correlations suggest neural principles of visual processing. Vis Cogn 2001;8(3/4/5):519–30.

Ermentrout GB, Kleinfeld D. Traveling electrical waves in cortex: insights from phase dynamics and speculation on a computational role. Neuron 2001;39:33–44.

Fabrigar LR, Wegener DT, MacCallum RC, Strahan EJ. Evaluating the use of exploratory factor analysis in psychological research. Psychol Methods 1999;4(3):272–99.

Freeman WJ, Barrie JM. Analysis of spatial patterns of phase in neocortical gamma EEGs in rabbit. J Neurophysiol 2000;84(3):1266–78.

Gratton G, Coles MG, Donchin E. A new method for off-line removal of ocular artifact. Electroencephalogr Clin Neurophysiol 1983;55(4):468–84.

Haig AR, Gordon E, Wright JJ, Meares RA, Bahramali H. Synchronous cortical gamma-band activity in task-relevant cognition. Neuroreport 2000;11:669–75.

Herrmann CS, Grigutsch M, Busch NA. EEG oscillations and wavelet analysis. In: Handy TC, editor. Event-related potentials: a methods handbook. Cambridge, Massachusetts: MIT Press; 2005. p. 229–59.

Horn JL. A rationale and technique for estimating the number of factors in factor analysis. Psychometrica 1965;30:179–85.

Hughes JR. The phenomenon of travelling waves: a review. Clin Electroencephalogr 1995a;26(1):1–6.

Hughes JR, Ikram A, Fino JJ. Characteristics of travelling waves under various conditions. Clin Electroencephalogr 1995b;26(1):7–22.

Humphreys LG, Ilgen DR. Note on a criterion for the number of common factors. Educ Psychol Meas 1969;29:571–8.

Ito J, Nikolaev AR, van Leeuwen C. Spatial and temporal structure of phase synchronization of spontaneous alpha EEG activity. Biol Cybern 2005;92(1):54–60.

Juergens E, Guettler A, Eckhorn R. Visual stimulation elicits locked and induced gamma oscillations in monkey intracortical- and EEG-potentials, but not in human EEG. Exp Brain Res 1999;129(2):247–59.

Kolev V, Yordanova J, Basar-Eroglu C, Basar E. Age effects on visual EEG responses reveal distinct frontal alpha networks. Clin Neurophysiol 2002;113(6):901–10.

Massimini M, Huber R, Ferrarelli F, Hill S, Tononi G. The sleep slow oscillation as a traveling wave. J Neurosci 2004;24(31):6862–70.

Nunez PL, Wingeier BM, Silberstein RB. Spatial–temporal structures of human alpha rhythms: theory, microcurrent sources, multiscale measurements, and global binding of local networks. Hum Brain Mapp 2001;13(3):125–64.

Rennie CJ, Wright JJ, Robinson PA. Mechanisms of cortical electrical activity and emergence of gamma rhythm. J Theor Biol 2000;205(1):17–35.

Ribary U, Ioannides AA, Singh KD, Hasson R, Bolton JP, Lado F, Mogilner A, Llinas R. Magnetic field tomography of coherent thalamocortical 40-Hz oscillations in humans. Proc Natl Acad Sci USA 1991;88(24):11037–41.

Rodriguez E, George N, Lachaux JP, Martinerie J, Renault B, Varela FJ. Perception's shadow: long distance synchronization of human brain activity. Nature 1999;397:430–3.

Roelfsema PR, Engel AK, Konig P, Singer W. Visuomotor integration is associated with zero time-lag synchronization among cortical areas. Nature 1997;385(6612):157–61.

Sauseng P, Klimesch W, Gruber W, Doppelmayr M, Stadler W, Schabus M. The interplay between theta and alpha oscillations in the human electroencephalogram reflects the transfer of information between memory systems. Neurosci Lett 2002;324(2):121–4.

Schack B, Rappelsberger P, Weiss S, Moller E. Adaptive phase estimation and its application in EEG analysis of word processing. J Neurosci Methods 1999;93(1):49–59.

Silberstein RB, Cadusch PJ. Measurement processes and spatial principal components analysis. Brain Topogr 1992;4(4):267–76.

Skrandies W, Lehmann D. Spatial principal components of multichannel maps evoked by lateral visual half-field stimuli. Electroencephalogr Clin Neurophysiol 1990;54(6):662–7.

Yordanova J, Kolev V, Heinrich H, Woerner W, Banaschewski T, Rothenberger A. Developmental event-related gamma oscillations: effects of auditory attention. Eur J Neurosci 2002;16(11):2214–24.

Yordanova JY, Kolev VN, Basar E. EEG theta and frontal alpha oscillations during auditory processing change with aging. Electroencephalogr Clin Neurophysiol 1998;108(5):497–505.